

# Volcanic Ash-Induced Decomposition of EB-PVD $\text{Gd}_2\text{Zr}_2\text{O}_7$ Thermal Barrier Coatings to Gd-Oxyapatite, Zircon, and Gd, Fe-Zirconolite

Peter Mechnich<sup>†</sup> and Wolfgang Braue

German Aerospace Center (DLR), Institute of Materials Research, Köln 51170, Germany

The resistance of EB-PVD  $\text{Gd}_2\text{Zr}_2\text{O}_7$  thermal barrier coatings against high-temperature infiltration and subsequent degradation by molten volcanic ash is investigated by microstructural analysis. At 1200°C, EB-PVD  $\text{Gd}_2\text{Zr}_2\text{O}_7$  coatings with silica-rich, artificial volcanic ash (AVA) overlay show a highly dynamic and complex recession scenario.  $\text{Gd}_2\text{O}_3$  is leached out from  $\text{Gd}_2\text{Zr}_2\text{O}_7$  by AVA and rapidly crystallizes as an oxyapatite-type solid-solution  $(\text{Ca},\text{Gd})_2(\text{Gd},\text{Zr})_8(\text{Si},\text{Al})_6\text{O}_{26}$ . The second product of  $\text{Gd}_2\text{Zr}_2\text{O}_7$  decomposition is  $\text{Gd}_2\text{O}_3$  fully stabilized  $\text{ZrO}_2$  (Gd-FSZ). Both reaction products are forming an interpenetrating network filling open coating porosity. However, first-generation Gd-oxyapatite and Gd-FSZ are exhibiting chemical evolution in the long term. The chemical composition of Gd-oxyapatite does evolve from Ca,Zr enriched to Gd-rich. AVA continuously leaches out  $\text{Gd}_2\text{O}_3$  from Gd-FSZ followed by destabilization to the monoclinic  $\text{ZrO}_2$  polymorph. Finally, zircon ( $\text{ZrSiO}_4$ ) is formed. In addition to the prevalent formation of Gd-oxyapatite, a Gd-, Zr-, Fe-, and Ti-rich oxide is observed. From chemical analysis and electron diffraction it is concluded that this phase belongs to the zirconolite-type family (zirconolite  $\text{CaZrTi}_2\text{O}_7$ ), exhibiting an almost full substitution  $\text{Ca}^{2+} + \text{Ti}^{4+} \rightleftharpoons \text{Gd}^{3+} + \text{Fe}^{3+}$ . As all  $\text{Gd}_2\text{Zr}_2\text{O}_7$  decomposition products with the exception of  $\text{ZrSiO}_4$  exhibit considerable solid solubility ranges, it is difficult to conclusively assess the resistance of EB-PVD  $\text{Gd}_2\text{Zr}_2\text{O}_7$  coatings versus volcanic ash attack.

## I. Introduction

AEROENGINES are prone to in-service degradation by the ingestion of airborne inorganic particles which are partially or fully melted in the combustion flame and subsequently deposited on hot surfaces. Evidently, the surfaces of first-stage high-pressure turbine blades and vanes are affected most severely. In most modern turbine engines these airfoils are protected by ~200- $\mu\text{m}$ -thick thermal barrier coatings (TBC) consisting of tetragonal, 7 wt%  $\text{Y}_2\text{O}_3$  partially stabilized  $\text{ZrO}_2$  (7-YSZ). Airfoil TBCs are fabricated by electron-beam physical vapor deposition (EB-PVD) which produces a characteristic columnar and highly porous microstructure showing beneficial strain tolerance.<sup>1</sup>

As airborne particles originate from geogenic sediments, their chemical composition typically reflects the chemical composition of sediment-forming oxide minerals. Dominating oxides are CaO, MgO,  $\text{Al}_2\text{O}_3$ , and  $\text{SiO}_2$ , hence this mechanism commonly is referred to as CMAS-type hot corrosion (CMAS = calcia–magnesia–alumina–silica). The CMAS-type hot corrosion of state-of-the-art EB-PVD 7-YSZ coatings has been examined extensively in field studies.<sup>2–6</sup> For laboratory

studies synthetic four-component CMAS exhibiting quasi-congruent melting at ~1240°C is frequently employed.<sup>7</sup> Upon melting, CMAS rapidly infiltrates columnar EB-PVD YSZ coatings. Ex-solution of  $\text{Y}_2\text{O}_3$  from tetragonal YSZ may lead to undesired, critical phase transformation to monoclinic  $\text{ZrO}_2$  (baddelyite) and cubic Ca,Y costabilized  $\text{ZrO}_2$ . CMAS infiltration of TBC porosity can cause severe mechanical stresses upon thermal cycling, eventually leading to crack formation and subsequent TBC spallation. An infiltration depth of 30  $\mu\text{m}$  has been considered as being critical.<sup>8</sup>

Among CMAS-type corrosion scenarios, ingestion and deposition of volcanic ashes (VA) rates as a severe threat to aeroengines.<sup>9–12</sup> VA include different proportions of major rock-forming minerals (alkaline-, alkaline-earth feldspars, pyroxenes, olivines, etc.) which are frequently embedded in  $\text{SiO}_2$ -rich glassy matrices. Thus, in addition to CMAS constituents, alkaline metal oxides ( $\text{Na}_2\text{O}$ ,  $\text{K}_2\text{O}$ ) and transition metal oxides ( $\text{FeO}$ ,  $\text{TiO}_2$ ) are abundant. Owing to their mineralogical complexity and a high silica-glass content VA typically exhibit a broad softening/melting range, which is in strong contrast to the quasi-congruent melting behavior of four-component CMAS.

Recently, we reported on 7-YSZ TBC recession experiments employing a sol-gel-derived artificial volcanic ash (AVA) matching the chemical composition of the Eyjafjallajökull (Iceland) volcanic ashes ejected during the spring 2010 eruption.<sup>13</sup> AVA is virtually amorphous and hence considered a well-suited model for genuine volcanic ashes melted in the turbine combustor prior to deposition on hot TBC surfaces. Annealing experiments using AVA/TBC diffusion couples revealed that even moderate temperatures of 1000°C and short times generated significant effects. In case of EBPVD-YSZ partial coating infiltration and significant Y-depletion of 7-YSZ was observed even at 1100°C. At 1200°C, almost full coating infiltration and partial decomposition of tetragonal 7-YSZ to monoclinic  $\text{ZrO}_2$  and formation of  $\text{ZrSiO}_4$  was observed.

The development of new TBC materials raises the question whether CMAS-type corrosion produces similar detrimental effects. Pyrochlore-type gadolinium zirconate ( $\text{Gd}_2\text{Zr}_2\text{O}_7$ ) is employed as next-generation “low  $\kappa$ ” TBC material.<sup>14,15</sup>  $\text{Gd}_2\text{Zr}_2\text{O}_7$  provides low-thermal conductivity, high phase stability, and low sintering kinetics as compared with the state-of-the-art tetragonal 7-YSZ.<sup>16</sup>

The thermochemical interaction of molten four-component CMAS and an EB-PVD  $\text{Gd}_2\text{Zr}_2\text{O}_7$  TBC was studied in laboratory by annealing at 1300°C.<sup>17</sup> After 4 h, an apatite-type  $\text{Ca}_2\text{Gd}_8(\text{SiO}_4)_6\text{O}_2$  phase (“Gd-oxyapatite”) and cubic Gd/Ca costabilized  $\text{ZrO}_2$  were found as crystalline reaction products at the CMAS/ $\text{Gd}_2\text{Zr}_2\text{O}_7$  interface. In contrast to standard EB-PVD YSZ coatings, infiltration of liquid CMAS was mitigated: the infiltration depth was limited to ~30  $\mu\text{m}$ . This favorable behavior is explained by rapid formation of crystalline reaction products sealing the pore channels of EB-PVD  $\text{Gd}_2\text{Zr}_2\text{O}_7$ .

A favorable mitigation of volcanic ash infiltration had been observed for APS  $\text{Gd}_2\text{Zr}_2\text{O}_7$  coatings as well.<sup>18</sup> In

D. J. Green—contributing editor

Manuscript No. 32081. Received September 21, 2012; approved January 28, 2013.

<sup>†</sup>Author to whom correspondence should be addressed. e-mail: peter.mechnich@dlr.de

analogy to the CMAS case, the decomposition of  $Gd_2Zr_2O_7$  to Gd-oxapatite and residual Gd-stabilized  $ZrO_2$  is considered being the key mitigation mechanism.

In the present work, we investigate the thermochemical interaction of EB-PVD  $Gd_2Zr_2O_7$  TBCs and AVA overlays upon isothermal annealing at 1200°C up to 100 h. We focus on the formation and stability of Gd-oxapatite and Gd-stabilized  $ZrO_2$  envisaged for long-term infiltration mitigation. The reaction sequence and microstructural development at the AVA/ $Gd_2Zr_2O_7$  interface is monitored by analytical electron microscopy. Supplementary experiments using powder mixtures are performed to verify reactions and phase relationships.

## II. Experimental Procedure

Approximately 220- $\mu$ m-thick  $Gd_2Zr_2O_7$  TBC were deposited by electron-beam physical vapor deposition (EB-PVD, von Ardenne Anlagentechnik, Dresden, Germany) on alumina substrates.  $Gd_2Zr_2O_7$  powders were synthesized using by codecomposition of  $Gd(NO_3)_3 \cdot 6H_2O$  and  $Zr(NO_3)_2 \cdot 4H_2O$  (Alfa Aesar, Karlsruhe, Germany), and subsequent annealing at 1200°C. Phase purity and crystallinity were confirmed by XRD analyses, respectively. The starting materials for the sol-gel synthesis of an artificial volcanic ash (AVA) were  $Al(NO_3)_3 \cdot 9H_2O$ ,  $Fe(NO_3)_3 \cdot 9H_2O$ ,  $Mg(NO_3)_2 \cdot 6H_2O$ ,  $Ca(NO_3)_2 \cdot 4H_2O$ ,  $NaNO_3$ ,  $KNO_3$ ,  $Mn(NO_3)_2 \cdot 4H_2O$ , tetra-ethyl orthosilicate (TEOS), tetra-ethyl orthotitanate (TEOT), and  $(NH_4)_2HPO_4$  (Merck, Darmstadt, Germany). After drying and annealing at 800°C AVA mostly is X-ray amorphous. The crystalline fraction predominantly consists of nanoscaled hematite  $Fe_2O_3$ . After ball-milling (Pulverisette 7 premium line, Fritsch, Idar-Oberstein, Germany), AVA basically exhibits a continuous grain-size distribution between 0.5 and 70  $\mu$ m, a maximum volume fraction at about 15  $\mu$ m, and a  $d_{50}$  value of  $\sim$ 12  $\mu$ m. Details of the preparation and characterization of AVA are given elsewhere.<sup>13</sup>

Diffusion couples were prepared by depositing about 20  $mg/cm^2$  of AVA powder on top of EB-PVD  $Gd_2Zr_2O_7$  coated coupons. All heat treatments were carried out in air in a resistor-heated chamber furnace (HTC 03/15, Nabertherm, Lilienthal, Germany) with annealing times of 0.1, 1, 10, and 100 h, respectively. A DSM Ultra 55 scanning electron microscope (SEM) (Carl Zeiss NTS, Wetzlar, Germany) equipped with an energy dispersive X-ray spectroscopy (EDS) system (Inca, Oxford Instruments, Abingdon, UK) was used for microstructural analyses. Focused ion beam (FIB)-assisted analytical transmission electron microscopy (TEM) was performed in a Strata 205 FIB system and a Tecnai F30 TEM-STEM utilizing a field-emission gun (FEI Inc., Eindhoven, The Netherlands). X-ray powder diffraction (XRD) (Siemens D5000,  $CuK\alpha$  radiation, and secondary graphite monochromator, EVA/Topas 4.2 software package, Bruker AXS, Karlsruhe, Germany) was used for phase analysis of powder samples.

## III. Results and Discussion

### (1) Microstructural Evolution of $Gd_2Zr_2O_7$ -TBC with AVA Deposits Upon Annealing at 1200°C for 0.1, 1, 10, and 100 h

The infiltration behavior, microstructural evolution, and reaction sequence at the AVA/ $Gd_2Zr_2O_7$  reaction front was studied by means of SEM and EDS analysis. A general feature of all SEM images is dark-contrasted areas associated with silica-rich, glaze-like AVA present as overlay and filling of TBC porosity. Faceted, light-contrasted grains growing in AVA are consisting predominantly of  $Fe_2O_3$ , along with some  $TiO_2$  and  $MgO$ , indicative of hematite-type solid solutions.

After annealing for 0.1 h at 1200°C, the development of a porous reaction zone at the top of the  $Gd_2Zr_2O_7$  columns is

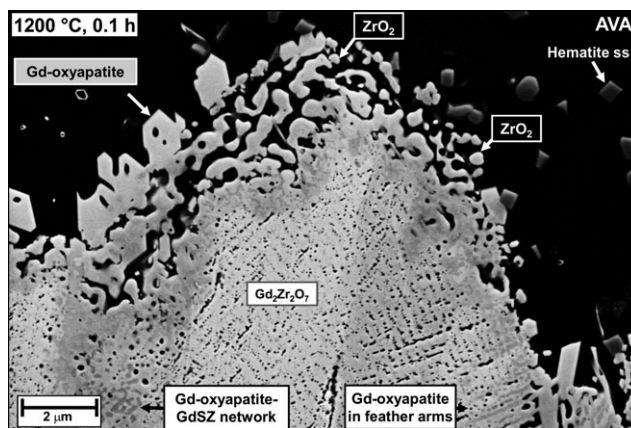


**Fig. 1.** SEM close-up of an EB-PVD  $Gd_2Zr_2O_7$  coating with AVA overlay upon annealing for 0.1 h at 1200°C. Adjacent to the AVA overlay, the  $Gd_2Zr_2O_7$  column tip shows an interpenetrating network of Gd-oxapatite and  $ZrO_2$ , a porous  $ZrO_2$  zone, and few faceted Gd-oxapatite grains. Note the undulated reaction front.

clearly visible (Fig 1). In addition, an extensive filling of  $Gd_2Zr_2O_7$  feather arms by a newly formed phase is obvious. Prismatic, light-contrasted grains with a size of 1–2  $\mu$ m are seemingly located at the initial  $Gd_2Zr_2O_7$ /AVA interface. EDS analyses revealed that these grains are Gd-oxapatite-type Ca-, Gd-silicate being the typical reaction product in the CMAS-type corrosion of  $Gd_2Zr_2O_7$ .<sup>17</sup> Below the Gd-oxapatite grains there exists a 2- $\mu$ m-thick zone characterized by nonfaceted 0.5–1  $\mu$ m  $ZrO_2$  grains enveloped by  $SiO_2$ -rich AVA. These  $ZrO_2$  grains are apparently residues of  $Gd_2Zr_2O_7$  decomposition. Right behind the well-defined, undulated reaction front there exists a zone of two differently contrasted phases. From the scenario observed on top of the coating it is concluded that this zone features an interpenetrating network of Gd-oxapatite and  $ZrO_2$  which is due to AVA infiltration of  $Gd_2Zr_2O_7$  feather-arm porosity and subsequent Gd-oxapatite formation.

Upon annealing for 1 h at 1200°C significant  $ZrO_2$  grain growth and pore coalescence has occurred in the recession zone (Fig. 2).  $ZrO_2$  grains are still blunted; some of them even exhibit droplet-like shapes. The pores are still filled with  $SiO_2$ -rich AVA. Gd-oxapatite is now predominantly found as large, platelet-like, and partially faceted grains growing in intercolumnar gaps of the EB-PVD coating. The interpenetrating network of Gd-oxapatite and  $ZrO_2$  now is clearly visible and the reaction front has moved considerably into

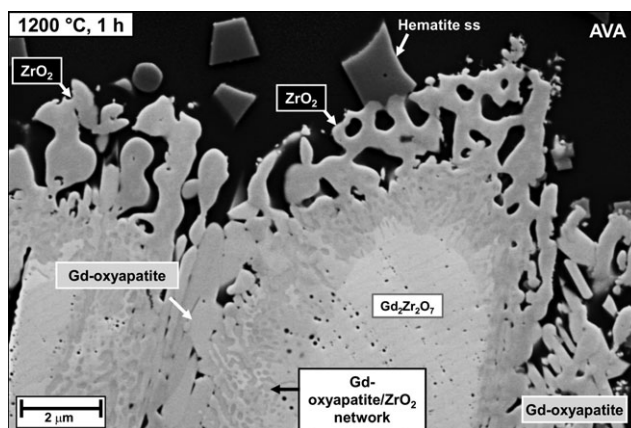


**Fig. 2.** EB-PVD  $Gd_2Zr_2O_7$  coating with AVA overlay upon annealing for 1 h at 1200°C. Significant  $ZrO_2$  grain growth and pore coalescence has occurred in the porous recession zone. Clearly visible are the interpenetrating Gd-oxapatite/ $ZrO_2$  network and platelet-like Gd-oxapatite grains located between  $Gd_2Zr_2O_7$  columns.

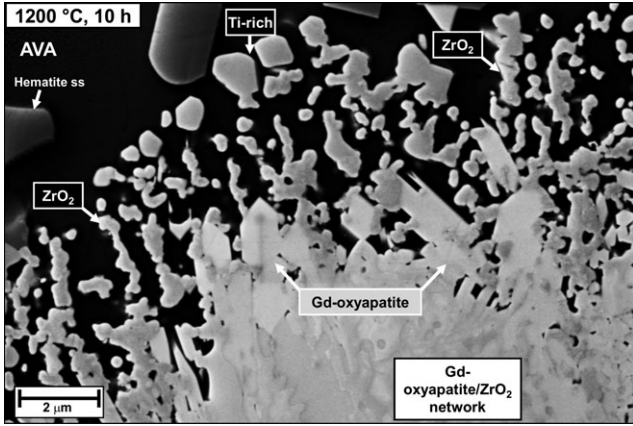


Fig. 3. EB-PVD  $Gd_2Zr_2O_7$  coating with AVA overlay upon annealing for 10 h at  $1200^\circ\text{C}$ .  $ZrO_2$  grains in the porous recession zone are much smaller. Gd-oxypatite grains now are exhibiting idiomorphic, hexagonal shapes. Ti-rich grains are arranged chain-like above the porous  $ZrO_2$  zone.

the  $Gd_2Zr_2O_7$  columns. Quantitative EDS analyses unambiguously revealed that in this reaction stage large  $ZrO_2$  grains have a composition of  $\sim 91$  mol%  $ZrO_2$  and 9 mol%  $Gd_2O_3$ , hence are cubic  $Gd_2O_3$  fully stabilized  $ZrO_2$  (Gd-FSZ). A costabilization with CaO, as observed by other authors in the CMAS case,<sup>17</sup> could not be proved unequivocally: EDS analysis yielded a value of  $\sim 0.3$  mol% CaO, evidently close to the detection limit.

Upon annealing for 10 h at  $1200^\circ\text{C}$  the recession zone is remarkably changing (Fig. 3): formerly large, blunted  $ZrO_2$  grains are now much smaller and consequently, the AVA-filled porosity has expanded significantly. Again, prismatic Gd-oxypatite grains are visible, but now are located at the interface of the porous AVA infiltrated zone and the Gd-oxypatite/Gd-FSZ interpenetrating network. Coarsening of Gd-oxypatite seems to occur within the Gd-oxypatite/Gd-FSZ network, observable at the bottom of Fig. 5. A new feature appears on top of the  $ZrO_2$ -dominated porous zone:  $0.2\text{--}1\ \mu\text{m}$  sized, faceted grains are arranged in an almost straight, chain-like manner. EDS analyses revealed a significant enrichment of Ti in these crystals.

Upon annealing for 100 h at  $1200^\circ\text{C}$  the microstructure of the reactive interface shows again a significant evolution (Fig. 4): small  $ZrO_2$  grains from the porous zone are

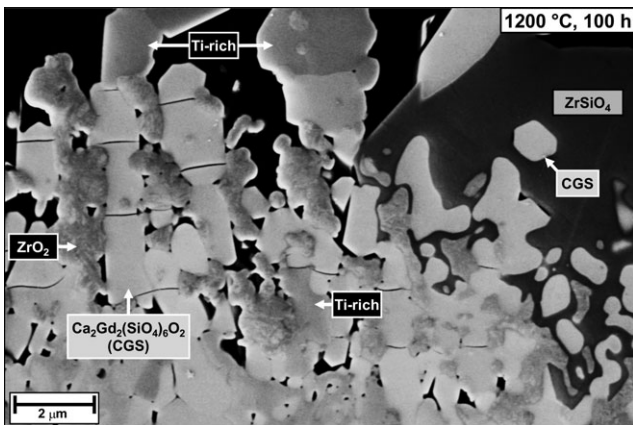


Fig. 4. EB-PVD  $Gd_2Zr_2O_7$  coating with AVA overlay upon annealing for 100 h at  $1200^\circ\text{C}$ . Small  $ZrO_2$  grains in the porous recession zone are now arranged in clusters and clearly show twin lamellae due to martensitic transformation. Large Gd-oxypatite grains are characterized by horizontal cracks. A large  $ZrSiO_4$  crystal has grown around Gd-oxypatite and m- $ZrO_2$ . Ti-rich grains are mostly localized on top of the reaction zone.

now arranged in clusters separated by large platelet-like Gd-oxypatite crystals. The  $ZrO_2$  grains clearly show twinning lamellae related to the martensitic transformation being distinctive for monoclinic  $ZrO_2$ . Horizontal segmentation cracks may occur in Gd-oxypatite crystals separating m- $ZrO_2$ . A newly appearing, darker contrasted phase exhibiting very large grains of  $10\ \mu\text{m}$  and beyond is identified by EDS as zircon  $ZrSiO_4$ . All  $ZrSiO_4$  grains are located directly on top of the former column tips and frequently show inclusions of Gd-oxypatite, occasionally m- $ZrO_2$  is observed too. The Ti-rich phase first observed in the sample annealed for 10 h appears typically as AVA-enveloped relative large-faceted grains in the upper region of the reactive interface, however, also directly in contact to Gd-oxypatite and m- $ZrO_2$ .

## (2) Phase Formation and Mitigation Performance at the AVA/ $Gd_2Zr_2O_7$ Interface

Figure 5 shows the time-dependent spatial distribution of silicon (bright contrasted) being representative for infiltrated silica-rich AVA. Evidently, infiltration of AVA is continuously increasing with time. Whereas only the topmost  $50\ \mu\text{m}$  of the EB-PVD  $Gd_2Zr_2O_7$  coating are affected after 0.1 h, the infiltration extends to more than  $150\ \mu\text{m}$  after 100 h at  $1200^\circ\text{C}$ . Despite a certain deceleration, there seems to be no full arrest of the infiltration front. This raises the question whether the concept of long-term infiltration mitigation by rapid formation of crystalline  $Gd_2Zr_2O_7$  decomposition products is viable. The microstructural evolution of the AVA/ $Gd_2Zr_2O_7$  diffusion couples indicates a highly complex reaction sequence.  $Gd_2Zr_2O_7$  decomposes to Gd-oxypatite and a  $Gd_2O_3$  fully stabilized  $ZrO_2$  (Gd-FSZ). Gd-oxypatite seems to form initially in  $Gd_2Zr_2O_7$  feather-arm porosity, but much larger, presumably second-generation apatites grow in the AVA overlay. A Ti-rich phase appears in intermediate reaction stages.  $ZrSiO_4$  appears in later reaction stages. An assessment of these observations is difficult without supplementary information on the constituents' crystal chemistry and phase stability. Therefore, we performed supplementary XRD, SEM, and TEM analyses.

(A) *Chemical Evolution of Gd-Oxypatite* Evidently, the formation of an interpenetrating Gd-oxypatite/GdSZ network designates the primary stage of AVA-related  $Gd_2Zr_2O_7$  decomposition. On the other hand, a porous GdSZ, AVA filled and almost Gd-oxypatite-free zone is observed in the top region which reasonably must be interpreted as the residuum of subsequent Gd-oxypatite decomposition, presumably via dissolution in AVA. In fact, higher magnification SEM imaging gives strong evidence for dissolution from first-generation apatite from the interpenetration network (Fig. 6). The undulated reaction front still contains Gd-oxypatite and Gd-FSZ with similar grain sizes. On top of this zone, much larger and blunted Gd-FSZ grains enveloped by AVA are visible, some of them obviously still separated by thin

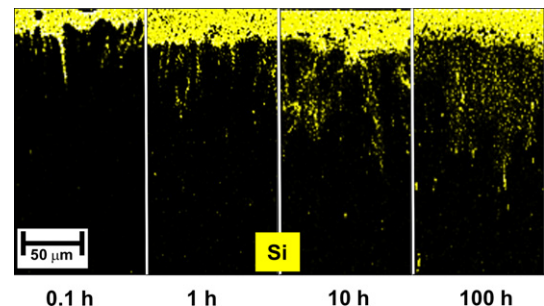


Fig. 5. EDS mapping of the EB-PVD  $Gd_2Zr_2O_7$  coating with AVA overlay upon annealing between 0.1 and 100 h at  $1200^\circ\text{C}$ . The spatial distribution of Si is indicative for a continuously increasing AVA infiltration.

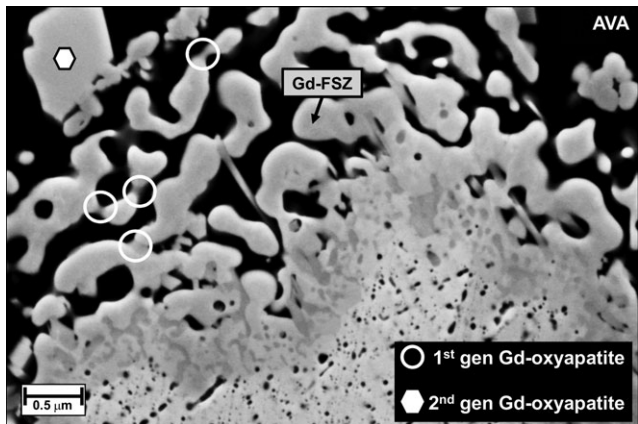


Fig. 6. Darker contrasted bridges between  $ZrO_2$  grains (open circles) provide strong evidence for dissolution of first-generation apatite out of the interpenetration network and subsequent free growth of idiomorphic second-generation apatite in AVA.

Gd-oxyapatite platelets (open circles) which obviously are the remains of Gd-oxyapatite dissolution. Coalescence and growth of Gd-FSZ are hence enhanced by disappearing Gd-oxyapatite grains. On the other hand, large-faceted Gd-oxyapatite grains are appearing in AVA close to the interface, i.e., only a few microns away there is obviously no driving force for dissolution. To study this seeming paradox we carried out a supplementary series of annealing experiments.

A phase pure, crystalline Gd-oxyapatite powder was synthesized at  $1300^\circ\text{C}$  using  $\text{Ca}(\text{NO}_3)_2 \cdot 4\text{H}_2\text{O}$ ,  $\text{Gd}(\text{NO}_3)_3 \cdot 6\text{H}_2\text{O}$  and fumed  $\text{SiO}_2$ . Gd-oxyapatite/AVA powder mixtures were annealed at  $1200^\circ\text{C}$  for 1 h, respectively. Figure 7 displays the XRD analyses of two selected powder mixtures. The 20/80 wt% mixture (Fig. 7, left hand side) exhibits Gd-oxyapatite XRD peaks in the initial state (lower XRD profile) as well after annealing at  $1200^\circ\text{C}$  (upper XRD profile). In addition, hematite has crystallized from AVA at  $1200^\circ\text{C}$ . On the contrary, only hematite is observed as crystalline phase after  $1200^\circ\text{C}$  annealing of the 10/90 wt% Gd-oxyapatite/AVA powder mixture (Fig. 7, right hand side). Evidently, Gd-oxyapatite has been completely decomposed due to AVA supersaturation. On the other hand, Gd-oxyapatite crystallizes if the local Gd content of AVA is exceeding

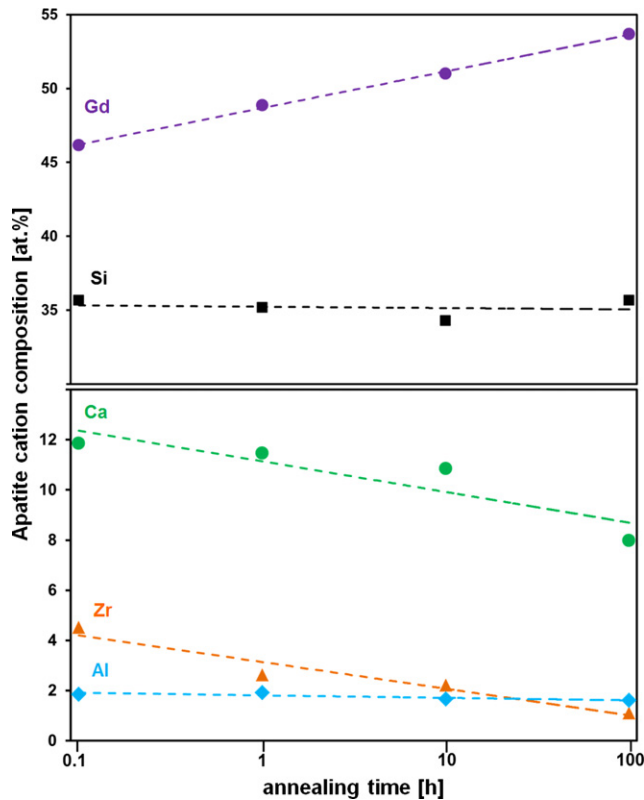


Fig. 8. Time-dependent evolution of the cation composition of Gd-oxyapatites upon annealing at  $1200^\circ\text{C}$  (normalized EDS data). A simultaneous decrease in Ca, Zr and increase in Gd is evident. (note logarithmic timescale).

the threshold for nucleation. This explains the rapid formation of first-generation Gd-oxyapatite preferably in feather-arm pores. The formation of the porous  $ZrO_2$  zone is hence due to the redissolution of first-generation Gd-oxyapatite, presumably caused by an evolving Gd-concentration gradient in AVA. Coexisting AVA is evidently becoming Gd-rich, providing stabilization of second-generation Gd-oxyapatite.

As silicate-apatite structures exhibit high chemical variability and significant solid solution ranges<sup>19</sup> and present

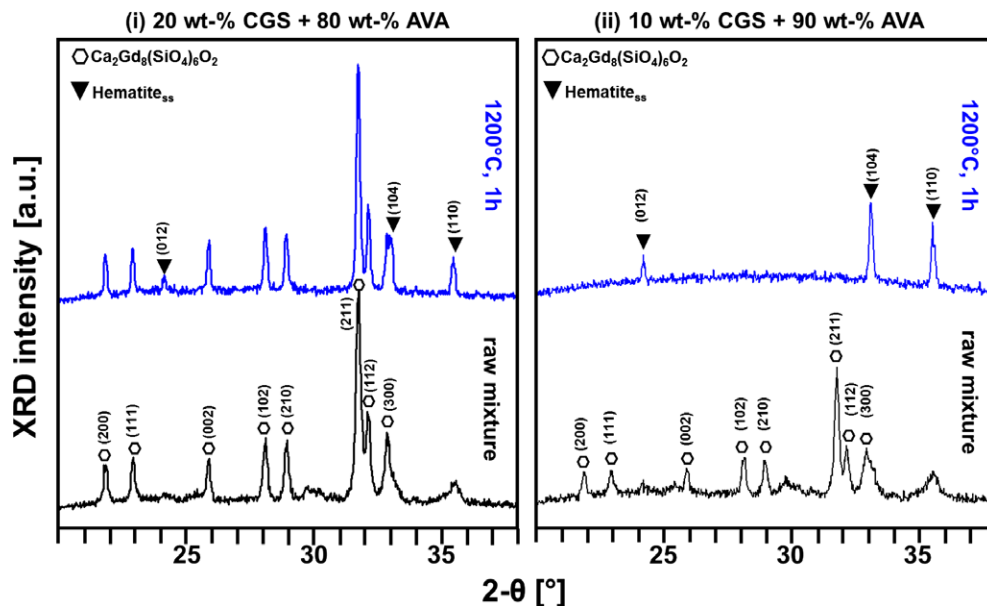


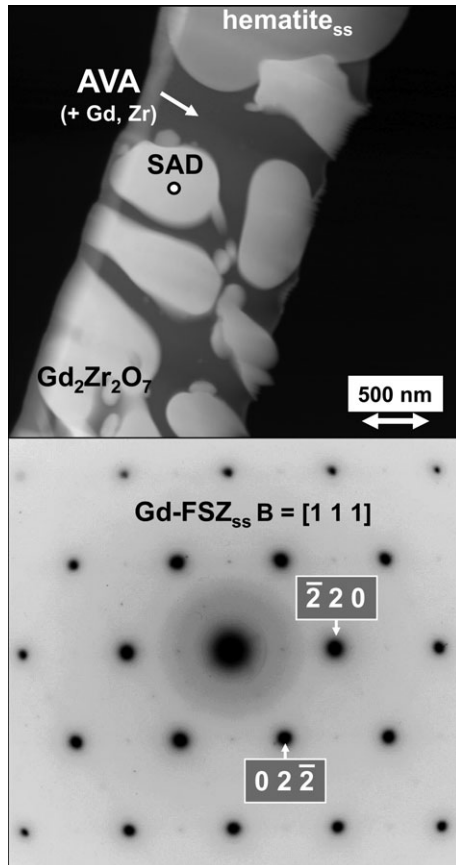
Fig. 7. XRD analysis of a 20/80 wt% Gd-oxyapatite/AVA mixture (left-hand) exhibits Gd-oxyapatite peaks in the initial state (lower profile) as well after annealing at  $1200^\circ\text{C}$  (upper profile) and hematite. Only hematite is observed as crystalline phase after  $1200^\circ\text{C}$  annealing of a 10/90 wt% Gd-oxyapatite/AVA powder mixture (right-hand). Gd-oxyapatite decomposition is due to AVA supersaturation.

**Table I. Calculation of Gd-Oxyapatite Crystal Chemistry from EDS Quantification**

| Cation       | $Ca^{2+}$ | $Gd^{3+}$ | $Zr^{4+}$ | $Si^{4+}$ | $Al^{3+}$ | Empirical Gd-oxyapatite                  |
|--------------|-----------|-----------|-----------|-----------|-----------|--|
| [at.%]       | 12.5      | 50.0      | –         | 37.5      | –         | $Ca_2Gd_8Si_6O_{26}$                     |
| Wyckhoff pos | $4f$      | $4f,6h$   | $6h$      | $6h$      | $6h$      | (hexagonal, space-group $P6_3/m$ (#176)) |

| Sample       | EDS data normalized to<br>(Ca + Gd + Zr) = 62.5 at.% |       |      | Normalized to<br>(Si + Al) = 37.5 |      | Gd-oxyapatite calculated from normalized EDS                                      |
|--------------|--|-------|------|-----------------------------------|------|---|
| 0.1 h/1200°C | 11.88  | 46.24 | 4.38 | 35.60                             | 1.90 | $(Ca_{0.95}Gd_{0.05})_2(Gd_{0.91}Zr_{0.09})_8(Si_{0.95}Al_{0.05})_6O_{26.25}$     |
| 1 h/1200°C   | 11.18  | 47.43 | 3.89 | 35.59                             | 1.91 | $(Ca_{0.9}Gd_{0.1})_2(Gd_{0.925}Zr_{0.075})_8(Si_{0.95}Al_{0.05})_6O_{26.25}$     |
| 10 h/1200°C  | 10.58  | 49.75 | 2.16 | 35.76                             | 1.74 | $(Ca_{0.85}Gd_{0.15})_2(Gd_{0.9625}Zr_{0.0375})_8(Si_{0.95}Al_{0.05})_6O_{26.15}$ |
| 100 h/1200°C | 7.94   | 53.74 | 1.09 | 35.88                             | 1.62 | $(Ca_{0.625}Gd_{0.375})_2(Gd_{0.98}Zr_{0.02})_8(Si_{0.95}Al_{0.05})_6O_{26.3}$    |



**Fig. 9.** Formation of Gd-doped fully stabilized zirconia (Gd-FSZ) next to hematite and  $Gd_2Zr_2O_7$  upon 1 h annealing (STEM high-angle annular dark-field (HAADF) image, upper part). [111] zone axis pattern obtained from Gd-FSZ grain marked (lower part).

Gd-oxyapatites coexist with chemically variable AVA, a chemical evolution upon annealing is anticipated for Gd-oxyapatites as well. Cross-sections of hexagonal basal planes of second-generation Gd-oxyapatite grains were exclusively selected for quantitative EDS spot analyses. Apart from the main constituents (Gd, Si, and Ca) we found significant dissolution of Zr in the apatite grains. This is in good agreement to the observations in the CMAS case,<sup>17</sup> where the authors detected 4–6 mol%  $ZrO_2$  dissolved in the Gd-oxyapatite structure at 1300°C. A significant Al content was detected as well. In contrast to data published by other authors for APS  $Gd_2Zr_2O_7$ /volcanic ash diffusion couples,<sup>18</sup> Mg and Fe dissolution in Gd-oxyapatite was found close to detection limits.

In Fig. 8 the mean relative content of apatite constituents is plotted versus the annealing time at 1200°C, respectively. Note that the timescale is logarithmic and only cations are considered. Evidently, there is a significant time-dependent evolution of the apatite's chemical composition. The Gd

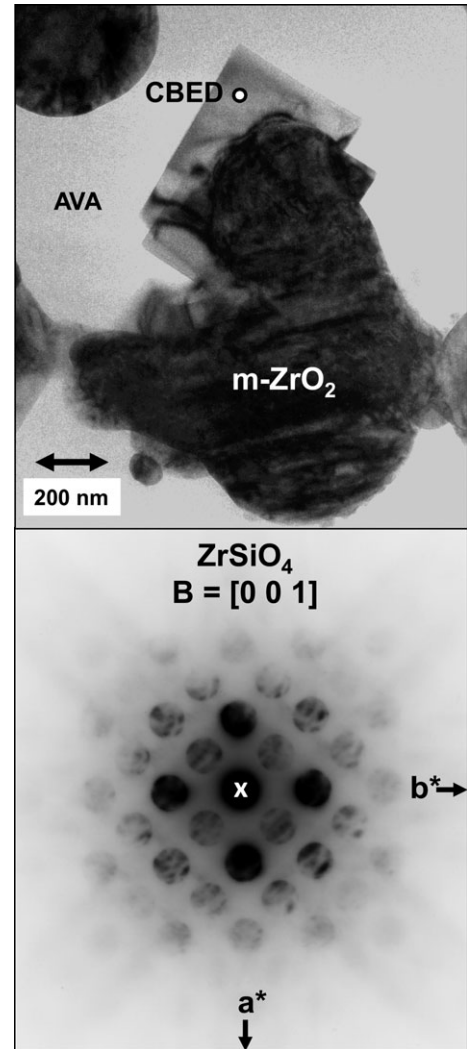


**Fig. 10.** Zircon ( $ZrSiO_4$ ) envelope established on twinned  $m$ - $ZrO_2$  upon 100 h annealing at 1200°C (bright-field (BF)-TEM, upper part). Convergent-beam electron-diffraction (CBED) pattern of zircon oriented parallel to the [001] zone axis (lower part).

content increases significantly from ~46.5 to 54 at.%, whereas Ca and Zr seem to decrease simultaneously from 12 to 8 and from 4.5 to 1 at.%, respectively. On the contrary, contents of Si (35 at.%) and minor Al (2 at.%) seem to remain almost constant. These EDS findings can be linked to apatite crystal chemistry: considering only cations and assuming a fully occupied apatite structure (space-group  $P6_3/m$ , no. 176) empirical Gd-oxyapatite ( $Ca_2Gd_8Si_6O_{26}$ ) includes 12.5 at.% Ca, 50 at.% Gd, and 37.5 at.% Si, respectively. Taking into account effective ionic radii,<sup>20</sup>  $Al^{3+}$  (0.039 nm) is obviously substituting  $Si^{4+}$  (0.026 nm) in tetrahedral

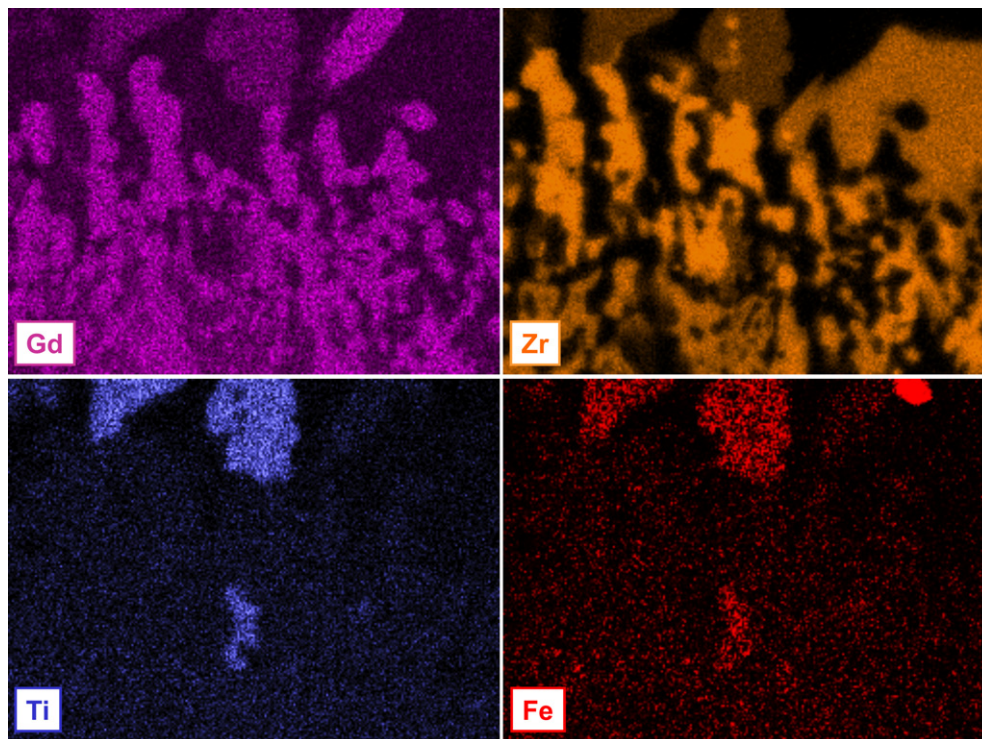


Fig. 11. EDS mapping of the EB-PVD  $Gd_2Zr_2O_7$  coating with AVA overlay (100 h at  $1200^\circ C$ , see Fig 4). Spatial element distribution shows accumulation of Gd, Zr, Ti, and Fe in an individual crystalline phase.

oxygen coordination. Charge balance may be achieved by coupled substitution of  $Ca^{2+}$  or  $Gd^{3+}$  by  $Zr^{4+}$ . Basically, the Gd-oxapatite lattice offers two sites occupied either predominantly by  $Ca^{2+}$  (Wyckhoff position 4 h, 8-fold coordinated by oxygen) or by  $Gd^{3+}$  (Wyckhoff 6f position, 7-fold coordinated by oxygen). From ionic radii data, it is anticipated that  $Zr^{4+}$  (0.078 nm) is rather substituting  $Gd^{3+}$  (0.100 nm) than  $Ca^{2+}$  (0.106 nm). Our model implicates that  $Al^{3+}$  and  $Si^{4+}$  add to 37.5 at.%, whereas  $Ca^{2+}$ ,  $Gd^{3+}$ , and  $Zr^{4+}$  sum up to 62.5 at.%. The EDS analyses were normalized with respect to these constraints and formulae of Gd-oxapatites were calculated, respectively (Table I). The observed Gd enrichment and simultaneous Ca depletion of oxapatites upon long-term annealing is hence explained by increasing substitution of  $Ca^{2+}$  by  $Gd^{3+}$  on position 4 h and simultaneous decreasing  $Zr^{4+}$  content on position 6f. Our data provide strong evidence that rapidly formed, first-generation Gd-oxapatite is metastable and hence does not provide a long-term stable AVA infiltration barrier.

**(B) Formation and Destabilization of  $ZrO_2$  Polymorphs** From the previous findings the destabilization of primary Gd-oxapatite by AVA is the most plausible rationale for the formation of a porous  $ZrO_2$  zone. In early stages of AVA infiltration the  $ZrO_2$  polymorph is still rich in  $Gd_2O_3$ . The chemical composition of Gd-FSZ (91.2 mol%  $ZrO_2$  and 8.8 mol%  $Gd_2O_3$ ) is indicative for a fully stabilized, cubic polymorph, which typically exhibits pronounced grain growth. However, the presence of much smaller, presumably monoclinic  $ZrO_2$  grains in later reaction stages indicates ongoing dissolution of  $Gd_2O_3$  from Gd-FSZ by AVA until transformation to m- $ZrO_2$  occurs.

At the end of this reaction sequence  $ZrSiO_4$  is formed at the expense of m- $ZrO_2$ , typically close to the porous zone.  $ZrSiO_4$  has also been observed as reaction product of EB-PVD 4 mol%  $Y_2O_3$ -stabilized  $ZrO_2$  (7-YSZ) TBCs and AVA, however, the formation was observed even upon annealing for only 1 h at  $1200^\circ C$ .<sup>13</sup> Obviously, the formation of  $ZrSiO_4$  is favored or even triggered by the destabilization of cubic or tetragonal  $ZrO_2$  to monoclinic  $ZrO_2$ . Destabilization is evidently much faster in case of 7-YSZ having a

relative low amount of solute serving as stabilizer. A detailed analysis by FIB-TEM was performed to disclose the evolution of the Gd-FSZ- $ZrSiO_4$  reaction sequence. Figure 9 (STEM HAADF) image shows the globular Gd-FSZ grains embedded in glassy AVA matrix along with residual  $Gd_2Zr_2O_7$  (bottom) and a hematite-type grain (top). The cubic structure obtained from electron diffraction (Fig. 9, bottom) proves the full stabilization of  $ZrO_2$  by  $Gd_2O_3$ . Figure 10 is representative for the decomposition of Gd-FSZ to globular destabilized m- $ZrO_2$  exhibiting characteristic twinning due to martensitic transformation. The prismatic grain enveloping globular m- $ZrO_2$  is unequivocally identified as  $ZrSiO_4$  by convergent-beam electron diffraction (CBED, Fig. 10, bottom). This scenario supports the concept of a  $ZrSiO_4$  formation from quasi fully destabilized m- $ZrO_2$  only. Again, our data prove that the first, rapidly formed decomposition product (Gd-FSZ) is not stable and not providing long-term mitigation of infiltration.

**(C) Identification and Analysis of a New, Zirconolite-Type Recession Product** Upon annealing at  $1200^\circ C$  for 10 and 100 h, a Ti-rich, obviously crystalline recession product was observed. The EDS mapping depicted in Fig. 11 shows the spatial distribution of Gd, Zr, Ti, and Fe in the area depicted in Fig. 4 (100 h  $1200^\circ C$  sample). Obviously, the Ti-rich phase holds Gd, Zr, and Fe as well. Spot analysis revealed also a low Al content: EDS quantification yielded a mean composition of ~30 at.% Zr, 24 at.% Gd, 21 at.% Ti, 20 at.% Fe, and 5 at.% Al, respectively (only cations considered). On the basis of this finding a literature review provided strong evidence that the unknown phase may belong to the zirconolite-type structure family. Zirconolite, having the idealized empirical formula  $CaZrTi_2O_7$  has been considered as potential host material for the immobilization of heavy radionuclides.<sup>21</sup> Interestingly,  $CaZrTi_2O_7$  or calzirtite ( $Ca_2Zr_5Ti_2O_{16}$ ) was recently detected on an ex-service EB-PVD 7-YSZ TBC, and their formation was explained by crystallization of Ti-bearing and Zr-enriched CMAS.<sup>22</sup> The zirconolite crystal structure is closely related to the pyrochlore-type structure family<sup>23,24</sup> and exhibits a large solubility for rare-earth as well as transition-metal

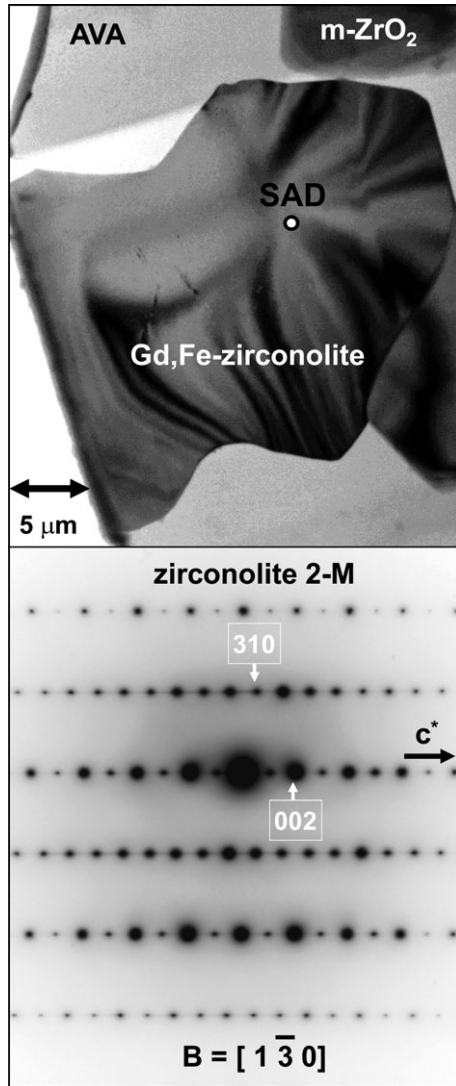


**Fig. 12.** Upper part: faceted Gd,Fe-zirconolite grain and m-ZrO<sub>2</sub> embedded in noncrystalline AVA upon 100 h annealing at 1200°C (BF-TEM). Lower part: [130] zone axis pattern of zirconolite confirming the monoclinic 2M polytype. Note extensive streaking parallel to c\*.

cations.<sup>25,26</sup> An isomorphous cosubstitution of zirconolite following  $Ca^{2+} + Ti^{4+} \leftrightarrow Gd^{3+} + Fe^{3+}$  has been proposed previously.<sup>27</sup> Uptake of  $Al^{3+}$  and an associated enrichment of  $Zr^{4+}$  above the “ideal” value of 1 has been considered as well. The crystal structure of Gd,Fe-substituted zirconolites was mostly found to be monoclinic, belonging to the space-group  $C2/m$  (no.12). In the present case, the above EDS analysis would translate to a charge-balanced, zirconolite-type solid solution with a composition close to  $Gd_{0.95}Zr_{1.15}Fe_{0.8}Ti_{0.9}Al_{0.2}O_7$ . To validate this hypothesis we performed FIB-TEM and electron diffraction. Figure 12 shows faceted zirconolite-type grains along with m-ZrO<sub>2</sub> embedded in glassy AVA. The related ED pattern (lower part) could be indexed successfully in monoclinic symmetry with lattice parameters close to those reported in literature. A characteristic streaking of the diffraction pattern parallel to c\* is observed in a similar manner to previous work.<sup>27</sup> To our best knowledge, we are reporting on such a Gd,Fe-zirconolite recession product for the first time in the open TBC literature. Interestingly, the formation of a garnet-type phase, in particular kimzeyite<sup>28</sup> was not observed although relative high amounts of major constituents, in particular, Ca, Zr, Ti, and Fe, are available in the present  $Gd_2Zr_2O_7$ -AVA system.

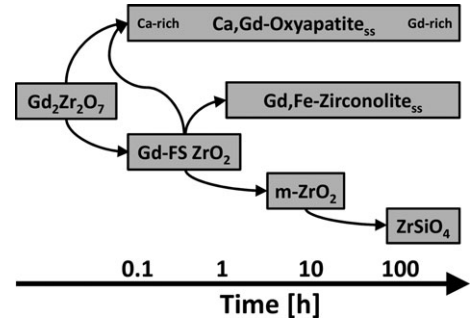


**Fig. 13.** Schematic of the  $Gd_2Zr_2O_7$ -AVA reaction sequence. (note logarithmic timescale)

### (3) Reaction Sequence and Possible Implications for Long-Term TBC Performance

Based on the microstructural analyses and the results retrieved from powder mixtures, it is possible to discriminate five key reaction stages explaining the recession scenario of EB-PVD  $Gd_2Zr_2O_7$  coatings with an artificial volcanic ash (AVA) overlay:

1.  $Gd_2O_3$  is leached out from  $Gd_2Zr_2O_7$  until AVA locally exceeds the  $Gd_2O_3$  concentration level required for nucleation of a Gd-oxyapatite solid solution. This process occurs rapidly inside of  $Gd_2Zr_2O_7$  feather-arm porosity. Progressive ex-solution of  $Gd_2O_3$  from  $Gd_2Zr_2O_7$  eventually leads to formation of cubic Gd-FSZ. Both primary decomposition products coexist as a kind of interpenetrating network.
2.  $Gd_2O_3$ -undersaturated AVA is able to selectively redissolve Gd-oxyapatite from the interpenetrating network. Residual, porous Gd-FSZ is filled with AVA and enhanced diffusion allows for Gd-FSZ grain coalescence and growth.
3. Large Gd-FSZ decomposes to small, globular, monoclinic  $ZrO_2$  via ex-solution of  $Gd_2O_3$ . Furthermore, Gd-oxyapatite destabilization is prevented by the  $Gd_2O_3$  enrichment of AVA, instead Gd-oxyapatite growth occurs.
4. A zirconolite-type phase containing  $Gd_2O_3$ ,  $ZrO_2$  originating from  $Gd_2Zr_2O_7$ , and  $TiO_2$ ,  $Fe_2O_3$  originating from AVA nucleates.
5. Large  $ZrSiO_4$  grains grow at the expense of small, globular, monoclinic  $ZrO_2$  grains and enveloping AVA.

A schematic of the reaction sequence is shown in Fig. 13. The fundamental driving force behind the observed phase formation may be the “de-mixing” of Gd and Zr into different siliceous environments: whereas Gd is preferably entering the oxyapatite structure, Zr is stabilized as  $ZrSiO_4$ . Due to coordination chemistry both crystal structures do not provide significant solubility for the other cation species. As a consequence it can be postulated that Gd and Zr coexist only in basically silica-free compounds such as  $Gd_2Zr_2O_7$ . Indeed, likewise the present zirconolite phase does not contain  $SiO_2$ . As  $Ti^{4+}$  does form titanates instead of silicates it is anticipated that the presence of  $Ti^{4+}$ , and to a lesser extent  $Fe^{3+}$ , is the major reason for the formation of Gd,Fe-zirconolite which can be regarded as derivative of  $CaZrTi_2O_7$ , i.e. zirconolite in sensu strictum. Taking into account these considerations, a long-term arrestment of the reaction front may be achieved only if the Si-rich AVA is mostly consumed.

As a deeper AVA infiltration and  $Gd_2Zr_2O_7$  decomposition is not prevented on the long term, thermophysical properties of newly formed crystalline phases are considered relevant for TBC performance. The influence of Gd-oxyapatite can be discussed in the light of literature data given for similar compounds of the apatite-type rare-earth silicate family. Work on isostructural, single-crystal  $Ca_2La_8(SiO_4)_6O_2$

revealed anisotropic coefficients of thermal expansion (CTE) of 8.9 ppm along the *a*- and 6.6 ppm along the *c*-axis, respectively.<sup>29</sup> This is considerably lower than the expansion of Gd<sub>2</sub>Zr<sub>2</sub>O<sub>7</sub> having a CTE of ~12 ppm. One can speculate that the horizontal cracks observed in large, elongated Gd-oxyapatite crystals (see Fig. 5) are due to a similar anisotropic CTE mismatch. In case of ZrSiO<sub>4</sub> the mismatch is even larger, with anisotropic CTE values of ~4.5 and 6.0 ppm for ZrSiO<sub>4</sub>, respectively.<sup>30</sup> Thermal expansion mismatches may produce mechanical stresses in the TBC upon thermal cycling which may cause coating exfoliation or spallation. Regarding the zirconolite-type phases, to date only CTE data for CaZrTi<sub>2</sub>O<sub>7</sub> are available: with ~12 ppm there is presumably no considerable CTE mismatch with Gd<sub>2</sub>Zr<sub>2</sub>O<sub>7</sub>.<sup>31</sup> Owing to their relative stability in the AVA environment and a close chemical as well as structural relationship with Gd<sub>2</sub>Zr<sub>2</sub>O<sub>7</sub>, such Gd,Fe-zirconolites may also be promising candidates for new, volcanic ash-resistant TBC materials.

#### IV. Conclusions

In a laboratory-scale approach we employed a sol-gel-derived, artificial volcanic ash (AVA) to study the possible long-term effects caused by the ingestion and subsequent deposition of volcanic ash particles on EB-PVD Gd<sub>2</sub>Zr<sub>2</sub>O<sub>7</sub> thermal barrier coatings. The thermochemical interaction of AVA and Gd<sub>2</sub>Zr<sub>2</sub>O<sub>7</sub> EB-PVD coatings is highly complex and exhibits features not seen before in similar, CMAS-type corrosion scenarios. Our observations indicate that a long-term mitigation of AVA infiltration may be not achievable for Gd<sub>2</sub>Zr<sub>2</sub>O<sub>7</sub> TBCs. This is mainly due to large solid-solution ranges of key reaction products, resulting in dynamic, permanently evolving chemical equilibria. Therefore, it seems mandatory to evaluate the concept of mitigation of infiltration by rapid decomposition/recrystallization of pyrochlore-type TBC materials via long-term annealing experiments, at least in the × 100 h range.

#### References

- <sup>1</sup>N. P. Padture, M. Gell, and E. H. Jordan, "Thermal Barrier Coatings for Gas-Turbine Engine Applications," *Science*, **296**, 280–4 (2002).
- <sup>2</sup>J. L. Smialek, F. A. Archer, and R. G. Garlick, "The Chemistry of Saudi Arabian Sand: A Deposition Problem on Helicopter Turbine Airfoils," pp. M63–77 in *3rd International SAMPE Metals and Metals Processing Conference*, Edited by F. H. Froes, W. Wallace, R. A. Cull and E. Struckhold, Toronto, Canada, 1992.
- <sup>3</sup>F. H. Stott, D. J. de Wet, and R. Taylor, "The Effect of Molten Silicate Deposits on the Stability of Thermal Barrier Coatings for Turbine Applications at Very High Temperatures," pp. M92–101 in *3rd International SAMPE Metals and Metals Processing Conference*, Edited by F. H. Froes, W. Wallace, R. A. Cull and E. Struckhold, Toronto, Canada, 1992.
- <sup>4</sup>D. J. de Wet, R. Taylor, and F. H. Stott, "Corrosion Mechanisms of ZrO<sub>2</sub>-Y<sub>2</sub>O<sub>3</sub> Thermal Barrier Coatings in the Presence of Molten Middle-East Sand," *J. Phys. IV*, **3** [C9] 655–63 (1993).
- <sup>5</sup>F. H. Stott, D. J. de Wet, and R. Taylor, "Degradation of Thermal-Barrier Coatings at Very High Temperatures," *MRS Bull.*, **19** [10] 46–9 (1994).
- <sup>6</sup>J. L. Smialek, F. A. Archer, and R. G. Garlick, "Turbine Airfoil Degradation in the Persian Gulf War," *J. Min. Metal. Mater. Soc.*, **46** [12] 39–41 (1994).
- <sup>7</sup>S. Krämer, J. Yang, C. G. Levi, and C. A. J. Johnson, "Thermochemical Interaction of Thermal Barrier Coatings with Molten CaO-MgO-Al<sub>2</sub>O<sub>3</sub>-SiO<sub>2</sub> (CMAS) Deposits," *J. Am. Ceram. Soc.*, **89** [10] 3167–75 (2006).

- <sup>8</sup>M. P. Borom, C. A. Johnson, and L. A. Peluso, "Role of Environmental Deposits and Operating Surface Temperature in Spallation of Air Plasma Sprayed Thermal Barrier Coatings," *Surf. Coat. Technol.*, **86–87**, 116–26 (1996).
- <sup>9</sup>J. Kim, M. G. Dunn, A. J. Baran, D. P. Wade, and E. L. Tremba, "Deposition of Volcanic Materials in the Hot Sections of Two Gas Turbine Engines," *J. Eng. Gas Turbines Power*, **115** [3] 641–51 (1993).
- <sup>10</sup>M. G. Dunn and D. P. Wade, "Influence of Volcanic Ash Clouds on Gas Turbine Engines", in *Volcanic Ash and Aviation Safety - Proceedings of the First International Symposium on Volcanic Ash and Aviation Safety*, Edited by T. J. Casadevall. *U.S. Geol. Survey Bull.*, **2047**, 107–18 (1994)
- <sup>11</sup>Z. J. Przedpelski and T. J. Casadevall, "Impact of Volcanic Ash from 15 December 1989 Redoubt Volcano Eruption on GE CF6-80C2 Turbofan Engines," *U.S. Geol. Survey Bull.*, **2047**, 129–35 (1994).
- <sup>12</sup>T. J. Grindle and F. W. Burcham Jr, *Engine Damage to a NASA DC-8-72 Airplane From a High-Altitude Encounter with a Diffuse Volcanic Ash Cloud*. NASA/TM-2003-212030, NASA Center for AeroSpace Information (CASI), Hanover, MD, 2003.
- <sup>13</sup>P. Mechnich, W. Braue, and U. Schulz, "High-Temperature Corrosion of EB-PVD Yttria Partially Stabilized Zirconia Thermal Barrier Coatings with an Artificial Volcanic Ash Overlay," *J. Am. Ceram. Soc.*, **94** [3] 925–31 (2011).
- <sup>14</sup>M. J. Maloney, "Thermal Barrier Coating Systems and Materials"; U.S. Patent 6,117,560, 2000.
- <sup>15</sup>R. Subramanian, "Thermal Barrier Coating Having High Phase Stability"; U.S. Patent 6,258,467, 2001.
- <sup>16</sup>C. G. Levi, "Emerging Materials and Processes for Thermal Barrier Systems," *Curr. Opin. Solid State Mater. Sci.*, **8**, 77–91 (2004).
- <sup>17</sup>S. Krämer, J. Yang, and C. G. Levi, "Infiltration-Inhibiting Reaction of Gadolinium Zirconate Thermal Barrier Coatings with CMAS Melts," *J. Am. Ceram. Soc.*, **91** [2] 576–83 (2008).
- <sup>18</sup>J. M. Drexler, A. D. Gledhill, K. Shinoda, A. L. Vasiliev, K. M. Reddy, S. Sampath, and N. P. Padture, "Jet Engine Coatings for Resisting Volcanic Ash Damage," *Adv. Mater.*, **23**, 2419–24 (2011).
- <sup>19</sup>J. Felsche, "Rare Earth Silicates with the Apatite Structure," *J. Solid State Chem.*, **5**, 266–75 (1972).
- <sup>20</sup>R. D. Shannon, "Revised Effective Ionic Radii and Systematic Studies of Interatomic Distances in Halides and Chalkogenides," *Acta Cryst.*, **32**, 751–67 (1976).
- <sup>21</sup>A. E. Ringwood, S. E. Kesson, N. G. Ware, W. Hibberson, and A. Major, "Immobilisation of High Level Nuclear Reactor Wastes in SYNROC," *Nature*, **278**, 219–23 (1979).
- <sup>22</sup>M. H. Vidal-Setif, N. Chellah, C. Rio, C. Sanchez, and O. Lavigne, "Calcium-Magnesium-Alumino-Silicate (CMAS) Degradation of EB-PVD Thermal Barrier Coatings: Characterization of CMAS Damage on Ex-Service High Pressure Blade TBCs," *Surf. Coat. Technol.*, **208**, 39–45 (2012).
- <sup>23</sup>T. White, "The Microstructure and Microchemistry of Synthetic Zirconolite, Zirkelite and Related Phases," *Am. Min.*, **69**, 1156–72 (1984).
- <sup>24</sup>P. Bayliss, F. Mazzi, R. Munno, and T. J. White, "Mineral Nomenclature: Zirconolite," *Min. Mag.*, **53**, 565–9 (1989).
- <sup>25</sup>H. J. Rossel, "Solid Solution of Metal Oxides in the Zirconolite Phase CaZrTi<sub>2</sub>O<sub>7</sub>. I. Heterotype Solid Solutions," *J. Solid State Chem.*, **99**, 38–51 (1992).
- <sup>26</sup>G. Della Ventura, F. Bellatreccia, and C. T. Williams, "Zirconolite with Significant REE<sub>2</sub>ZrNb(Mn,Fe)O<sub>7</sub> from a Xenolith of the Laacher See Eruptive Center, Eifel Volcanic Region, Germany," *Can. Min.*, **38**, 57–65 (2000).
- <sup>27</sup>S. V. Stefanovsky, A. Y. Troole, M. I. Lapina, B. S. Nikonov, A. V. Sivtsov, and S. V. Yudinstevev, "XRD, SEM and TEM Study of the Gd-Doped Zirconolites"; in *Scientific Basis for Nuclear Waste Management*, B. P. McG-rail, *Mat. Res. Soc. Symp. Proc.*, **717**, 345–50 (2002).
- <sup>28</sup>W. Braue and P. Mechnich, "Recession of an EB-PVD YSZ Coated Turbine Blade by CaSO<sub>4</sub> and Fe,Ti-Rich CMAS-Type Deposits," *J. Am. Ceram. Soc.*, **94** [12] 4483–9 (2011).
- <sup>29</sup>R. H. Hopkins, J. de Klerk, P. Piotrowski, M. S. Walker, and M. P. Mathur, "Thermal and Elastic Properties of Silicate Gd-Oxyapatite Crystals," *J. Appl. Phys.*, **44** [6] 2456–8 (1973).
- <sup>30</sup>Z. Mursic, T. Vogt, and F. Frey, "High-Temperature Neutron Powder Diffraction Study of ZrSiO<sub>4</sub> up to 1900 K," *Acta Cryst.*, **48**, 584–90 (1992).
- <sup>31</sup>C. J. Ball, G. J. Thorogood, and E. R. Vance, "Thermal Expansion Coefficients of Zirconolite (CaZrTi<sub>2</sub>O<sub>7</sub>) and Perovskite (CaTiO<sub>3</sub>) from X-Ray Powder Diffraction Analysis," *J. Nucl. Mat.*, **190**, 298–301 (1992). □